140-GHz Wideband Array Antenna-in-Package Using Multimode Resonance

Hyunjin Kim, *Member, IEEE*, and Jungsuek Oh, *Senior Member, IEEE*

***Abstract*— A 140-GHz wideband array antenna-in-package (AiP) that uses multimode resonance is proposed based on a low-profile multilayer printed circuit board (PCB), which can be incorporated with flip-chip technology and an integrated transceiver. Using the multiple resonances of a patch and λ/4 monopole-type feeder, a simulated impedance bandwidth of 53% and stable radiation performance over the operating band were achieved. A 4 × 4 antenna array achieves a gain of up to 18.1 dBi, a radiation efficiency of 80%, and a cross-polarization discrimination (XPD) of over 20 dB. By combining the elements with a feed network composed of striplines, single and 4 × 4 antenna arrays were designed and fabricated. The capacitance caused by the limitations of the fabrication process was analyzed and overcome using a novel capped-cavity structure. From the experiment, a −10 dB impedance bandwidth of 31% was measured.**

***Index Terms*— Antenna array, D-band, multilayer PCB, sixth-generation (6G), via transition.**

I. Introduction

D-BAND frequencies (ranging from 110 to 170 GHz) have received considerable attention owing to the wide bandwidth. Radar transceivers are used in industrial applications that require scientific and medical bands, such as 122 GHz, to achieve a wide bandwidth for high-resolution radar systems [1], [2], [3]. Moreover, the D-band frequency is a candidate frequency spectrum for sixth-generation (6G) communication systems [4], [5], [6]. Despite the application of D-band for satellites, terrestrial exploration, and so on, there are vast wideband channels, including 130–134, 141–148.5, and 151.5–164 GHz [7]. These wide bandwidths allow for the 6G requirement of the Tbps data rate. The opening of the frequency range between 95 and 3000 GHz by the Federal Communications Commission (FCC) for trial applications also motivates the development of advanced millimeter-wave (mmWave) communication technologies [8]. Therefore, it is necessary to study and develop wideband antenna elements.

Several studies have been conducted on the design of wideband antennas in the multilayered fabrication process in the D-band. Substrate-integrated waveguide (SIW)-fed antennas [9], [10] were designed using a low-temperature co-fired ceramic (LTCC) substrate. In [11], a D-band resonant cavity antenna with a bandwidth of 14.2% was fabricated using 3-D printing methods was presented. In [12], an impedance bandwidth of 42.8% was achieved using multiple high-order modes of the SIW-fed slot antenna. However, these antennas are fed by waveguides and cannot be interconnected using mmWave radio-frequency integrated circuits (RFICs). Most antennas for silicon-based mmWave modules are designed and integrated through a multilayered fabrication process with the interconnection of an RFIC [13], [14], [15]. This is because antenna-in-package (AiP) can reduce interconnection loss, making the packaging effective and increasing manufacturing reliability. In addition, AiPs can be scalably extended if they are connected to an RFIC using flip-chip bonding.

For lower mmWave frequencies, several types of wideband antennas that can be interconnected with RFICs have been studied and reported. An LTCC L-probe feed patch antenna with an impedance bandwidth of 29% (53–71 GHz) and a soft-surface structure that suppresses the substrate surface wave was reported [16]. Several types of wideband patch antennas, such as circular pad or L-probe-fed antennas, have been proposed [17], [18]. Magnetoelectric (ME) dipole antenna is widely studied because its broad bandwidth is realized by combining an electric dipole and a short patch antenna [19], [20], [21]. The ME dipole antennas fed by L-shaped probes have impedance bandwidths of 51% (46–70 GHz) [19] and 42.5% (25.5–40.2 GHz) [21].

This article presents a wideband patch antenna that uses multimode resonance and is organized as follows. Section II presents the multilayer printed circuit board (PCB) layer configuration and design rules. The design of the antenna element and its operating principles are also presented. Section III presents the 4 × 4 array antenna performance and analysis. In Section IV, a new feedline design is proposed to overcome the high capacitance, and it is validated using the experimental results. Finally, conclusion is presented in Section V.

II. Antenna Element Design

A. Antenna Configuration

Typical PCB manufacturing processes have difficulty satisfying the requirements of integrating antenna arrays operating

Manuscript received 7 September 2022; revised 5 December 2022; accepted 11 December 2022. Date of publication 24 January 2023; date of current version 6 March 2023. This work was supported in part by the Institute of Information and Communications Technology Planning and Evaluation (IITP) Grant funded by the Korean Government through Ministry of Science and ICT (MSIT) (Innovative Fusion Technologies of Intelligent Antenna Material/Structure/Network for THz 6G) under Grant 2021-0-00763 and in part by the Basic Science Research Program through the National Research Foundation of Korea (NRF) funded by the Ministry of Education under Grant 2022R1A6A3A01085999. *(Corresponding author: Jungsuek Oh.)*

The authors are with the Department of Electrical and Computer Engineering, Institute of New Media and Communications (INMC), Seoul National University, Seoul 08826, South Korea (e-mail: hyzinki@snu.ac.kr; jungsuek@snu.ac.kr).

Color versions of one or more figures in this article are available at https://doi.org/10.1109/TAP.2023.3237162.

Digital Object Identifier 10.1109/TAP.2023.3237162

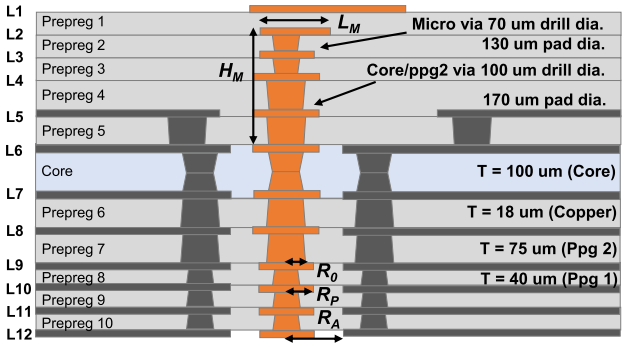

Fig. 1. Antenna layer structure in advanced multilayer PCB technology.

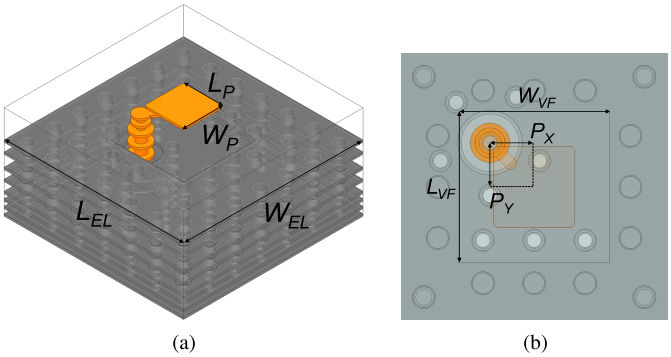

Fig. 2. (a) Bird's eye view and (b) top view of antenna element design.

at the D-band frequency, which have minimum trace and spacing widths of approximately 50–100 μm and a minimum diameter of approximately 75–100 μm. Under these conditions, it is difficult to realize its configuration via transition from the RFIC, and the ground space is insufficient to draw signal traces and power lines. However, a multilayer PCB fabrication process has been established, and advanced technology can provide a minimum trace width and spacing of 30 μm. The via and pad diameters differ depending on the thickness of the core and the preimpregnated (prepreg or ppg) layers, which are presented in Fig. 1. The PCB consists of 12 layers: metallization, core, prepreg, and laser microvias. The steps in the fabrication process are illustrated in [22]. The process begins with the core, and the prepreg functions as an adhesive to stick the substrates together. After the prepreg solidifies, the metal routes or laser-drilled microvias are fabricated. In this study, although the drilling of the plated through-holes was used as the core substrate, both sides of the core substrate were laser-drilled, and cone-shaped microvias were used. The relative dielectric permittivity (ε_r) of the core and prepreg substrate was 3.4 and 3.2, respectively, and the loss tangent of both substrates was 0.004.

Fig. 1 shows the cross section of the via transition from the bottom metal layer to the upper layers, comprising several via holes and capture pads. The capacitances of the model shown in Fig. 1 are the pad barrel-to-plate coaxial capacitances, C_{BP}, the via barrel-to-plate capacitances, C_{VP}, and fringing capacitances, C_f [23]. The capacitances C_{BP} and C_{VP} can be obtained by [24], [25], [26]

$$C_{BP} = \frac{2\pi\varepsilon_r\varepsilon_0 T}{\ln(R_A/R_P)} \tag{1}$$

$$C_{VP} = \frac{\pi\varepsilon_r\varepsilon_0 h B_0}{\ln(R_A/R_0)} \tag{2}$$

where B_0 is the constant coefficient and T and h are the thicknesses of the copper layer and substrate, respectively, which indicate that the capacitance increases with increasing T and h. From the equations, a larger antipad radius R_A, smaller capture pad radius R_P, and smaller via radius R_0 are required to achieve a smaller capacitance. Although advanced multilayer PCB technology can reduce the capacitance using a finer fabrication process, the capacitance can affect the performance of the antenna in the D-band. The antenna element design is demonstrated by considering the capacitance, as shown in Fig. 1.

The ANSYS electromagnetic (EM) simulation model of the antenna element is shown in Fig. 2 with a bird's eye and top view. The antenna consists of a patch, a monopole-type feeder, and a via the fence. For 45° slant polarization, the feeder was located at the corner of the patch. Although an L-probe patch antenna typically uses 0.1 0.15λ_0 [16], the antenna is designed using a feeder with a height of $\lambda_g/4$ to achieve a wider bandwidth. The antenna design parameters are shown in Figs. 1 and 2, which are the height of the feeder, $H_M = 0.302$ mm, length of the probe, $L_M = 0.16$ mm, width of the patch, $W_P = 0.35$ mm, length of the patch, $L_P = 0.35$ mm, width of the via fence, $W_{VF} = 0.65$ mm, length of the via fence, $L_{VF} = 0.65$ mm, and position of the feeder, $P_X = P_Y = 0.19$ mm.

B. Antenna Operation Principle

In Fig. 3, the layer structures of various antenna types are shown, and the real part of the input impedance is plotted to compare the resonant antenna modes. The patch antenna with direct feed shown in Fig. 3(a) is designed to resonate at a low D-band (110–120 GHz), as plotted, and a top-loaded $\lambda_g/4$ monopole antenna in Fig. 3(b) is designed to resonate at the mid-D-band (140–150 GHz), as shown. The proposed antenna, as shown in Fig. 3(c), is designed to incorporate both a coupled feed patch antenna and $\lambda_g/4$ monopole antenna; hence, a wideband characteristic can be achieved with a combination of two antenna resonant modes and higher-order modes, as shown in Fig. 3(e), respectively. The stacked patch antenna shown in Fig. 3(d) was designed for comparison with the proposed antenna [27], [28], [29], [30]. Although the stacked patch antenna also exhibits additional resonance, its bandwidth is narrower than that of the proposed antenna. The monopole-type feeder of the proposed antenna can provide a wider bandwidth than the coupled feed structure of the stacked patch antenna.

The electric field distributions of the proposed antenna are shown in Fig. 4 from 120 to 160 GHz. The electric-field distribution of the patch antenna TM_{10} mode can be observed at 120 GHz, as shown in Fig. 3(a), whereas the electric-field distribution at 140 GHz in Fig. 3(b) and 160 GHz in Fig. 3(c) approaches a top-loaded monopole-type antenna mode at 160 GHz in Fig. 3(d).

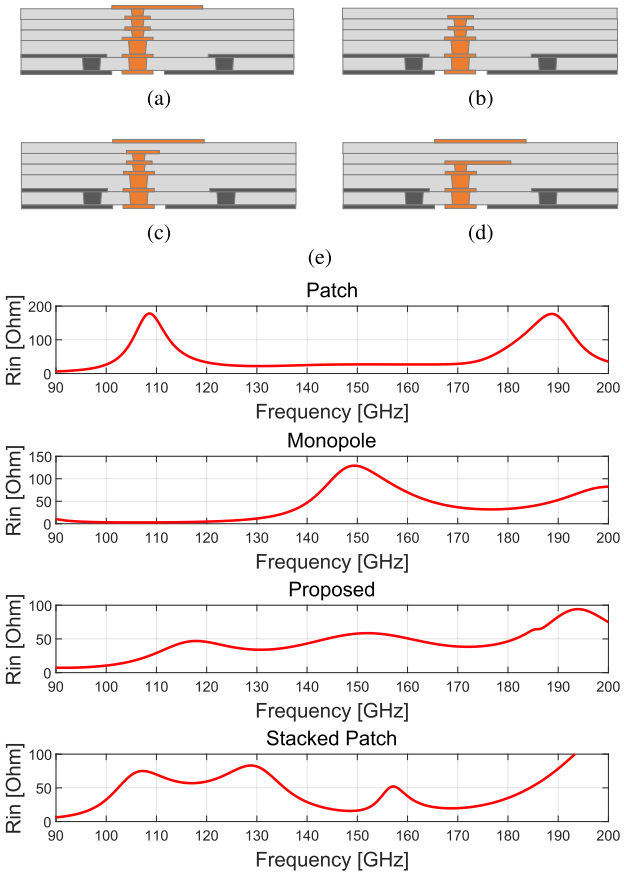

Fig. 3. Layer structure of (a) patch, (b) monopole, (c) proposed, and (d) stacked patch antenna. (e) Compared real part of the input impedance of various types of antennae.

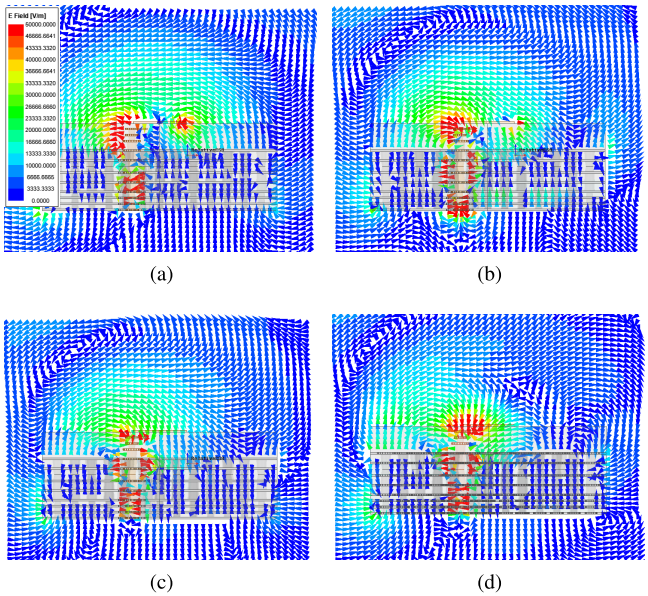

Fig. 4. Electric field distributions of the proposed antenna at (a) 120, (b) 140, (c) 160, and (d) 160 GHz without a patch.

C. Parametric Studies and Performance

S_{11} of the proposed antenna is shown in Fig. 5 according to the patch size variation and heights of the monopole feeder. The resonant mode of the proposed antenna without a patch is approximately 160 GHz, and the reflection coefficient smaller

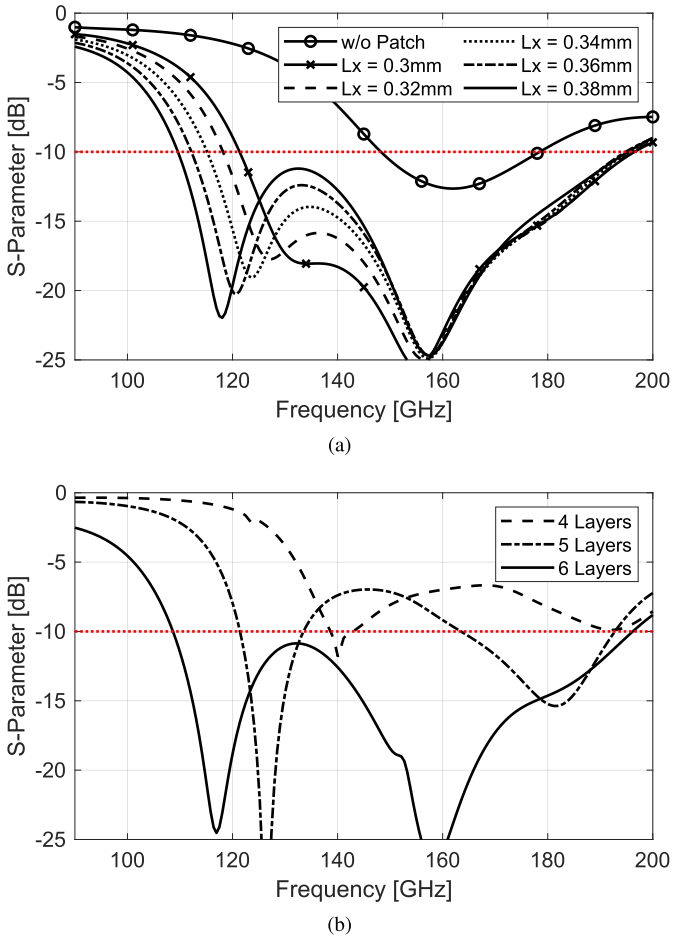

Fig. 5. S_{11} of the proposed antenna according to (a) patch size variation and (b) heights of the monopole feeder.

than -10 dB ($S_{11} < -10$ dB) is between 145 and 180 GHz, as shown in Fig. 5(a). An additional resonant mode can be created with a coupled feed patch and adjusted with a patch size variation. In Fig. 5(b), the S_{11} values of the different antenna heights and feeders are plotted. With a decrease in the total number of antenna layers from 6 to 4, the height of the antenna feeder also decreases from 0.302 to 0.116 mm. As the height of the monopole-type feeder decreases, the resonant frequency increases, and the bandwidth of the total reflection coefficients decreases. The antenna design and operation using multimode resonances are confirmed from the simulation results.

In Fig. 6(a), the S_{11} parametric results of the proposed antenna are plotted according to the length of the probe feeder. As the length of the probe feeder increases, inductive coupling between the probe and patch increases, and the resonant mode shifts to a lower frequency. In addition, the monopole resonant mode shifts to a lower frequency with an increase in the length, and the reflection coefficient decreases with an increase in inductance. S_{11} of the proposed antenna is shown in Fig. 6(b) according to the position of the monopole feeder. As the position of the feeder moves outward from the patch, the coupling points between the probe and patch move outward from the patch, and the frequency of the resonant mode decreases. In addition, the monopole resonant mode shifts to a higher frequency because the coupling between the feeder and

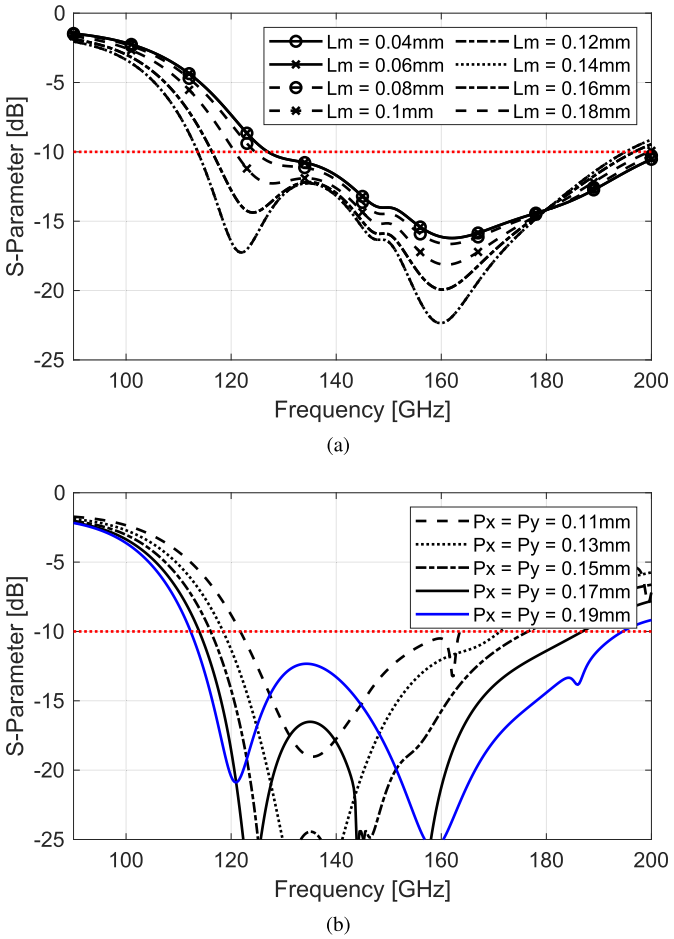

Fig. 6. S_{11} of the proposed antenna according to (a) lengths of the probe feeder and (b) position of the monopole feeder.

the patch decreases; therefore, a lower reflection coefficient and wider bandwidth can be achieved.

The radiation patterns of the proposed antenna elements are shown in Fig. 7. The width and length of the element ground size, $L_{EL} = W_{EL} = 1.6$ mm, are determined as $0.75\lambda_0$ at 140 GHz to provide suitable antenna gain. The maximum antenna gain can be stably maintained at approximately 5.5 dBi from 120 to 170 GHz. The half-power beam widths (HPBWs) are maintained at approximately 85°. As the frequency increases, the radiation pattern becomes sharper with an increase in the relative ground size.

III. Antenna Array Performance

A 4 × 4 array antenna was designed to verify array performance, as shown in Fig. 8. The element spacing was determined as 1.2 mm, which is $0.56\lambda_0$ at 140 GHz. Half of the antenna array was rotated by 180° to achieve higher cross-polarization discrimination (XPD) and port-to-port isolation [31], [32]. The via fences were also incorporated from the antenna element design stage, which can improve port-to-port isolation; hence, the antenna array performance can improve the realized gain and bandwidth [33], [34]. A via fence with a lower height was used to achieve a wider bandwidth, as shown in Fig. 1. The S-parameters and realized gain of the antenna array with and without the via fences are plotted against the

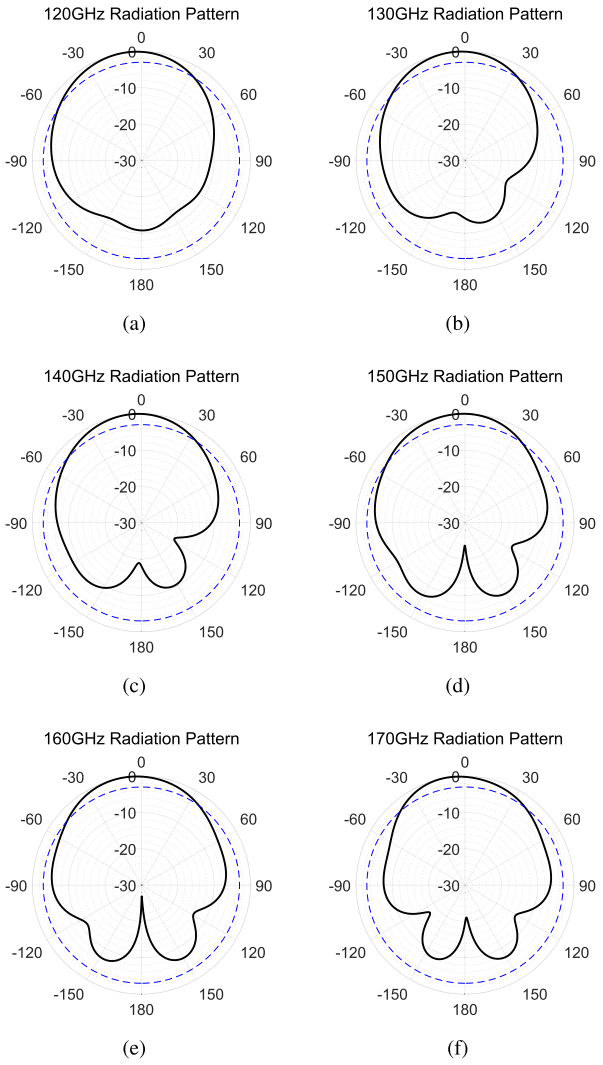

Fig. 7. Radiation patterns of antenna element at (a) 120, (b) 130, (c) 140, (d) 150, (e) 160, and (f) 170 GHz.

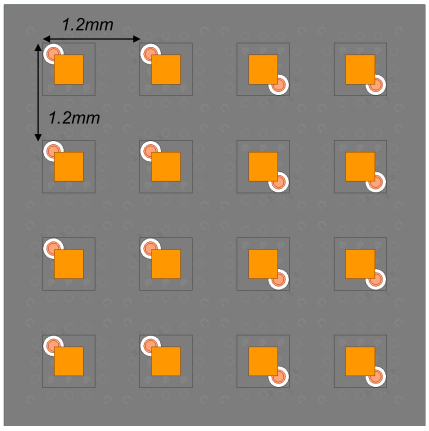

Fig. 8. Antenna array configuration with rotated feeders.

frequency in Fig. 9. The isolation, reflection coefficients, and realized gain deteriorate without the via fences because of the surface wave along the ground plane. In particular, S_{11} of the monopole mode resonance at a higher frequency decay severely. However, a better performance of S_{11} is established, and the realized gain can be achieved using via fences. Both

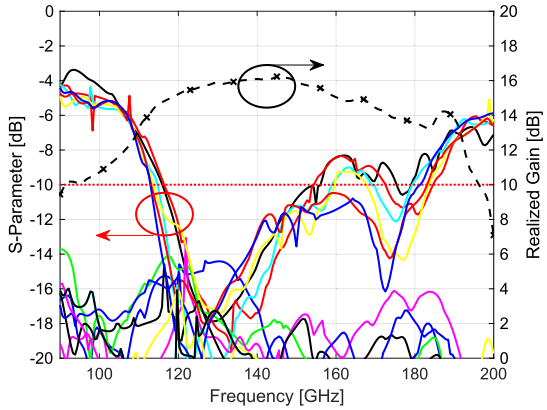

(a)

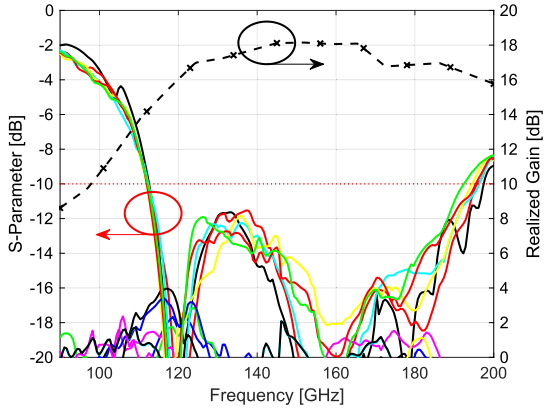

(b)

Fig. 9. S-parameters and realized gain of the antenna array (a) without via fences and (b) with via fences.

the S_{11} bandwidth and 3 dB gain bandwidth are greater than 70 GHz (120–190 GHz). Although a via fence is used with a lower height, a port-to-port isolation higher than 15 dB can be achieved. If greater isolation is required, the height of the via fence can be adjusted.

The radiation patterns of the antenna array are plotted at 120, 145, and 170 GHz, as shown in Fig. 10(a)–(c), respectively. The relative element spacing with 1.2 mm becomes $0.48\lambda_0$, $0.58\lambda_0$, and $0.68\lambda_0$ at each frequency, respectively. From the beamformed radiation patterns in the figure, the 6 dB beam coverage is reduced from ± 64 to $\pm 50°$, as the relative element spacing increases. With a 180° physical rotation of half the number of antenna arrays, as shown in Fig. 8, a high-boresight XPD of over 25 dB can be achieved for all frequencies.

IV. Feedline Design and Validation

A. Feedline Design

A stripline is designed to interconnect the antenna element and the RFIC, as shown in Fig. 11. The stripline is located between layers 9 and 11, and the other RF routings can be situated from layers 6 to 12. The via transitions are also adapted to connect the bottom to the upper layers. The capacitance between the capture pads and the ground plane can be a bottleneck for performance in terms of bandwidth.

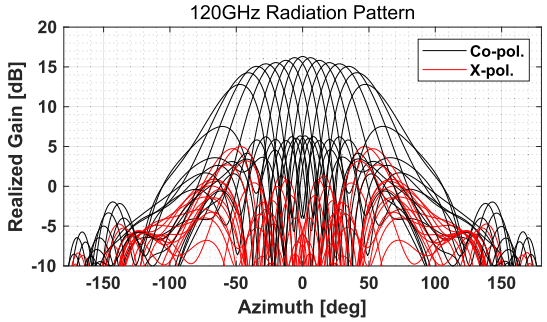

(a)

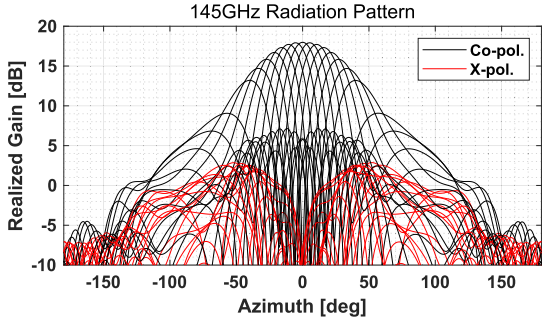

(b)

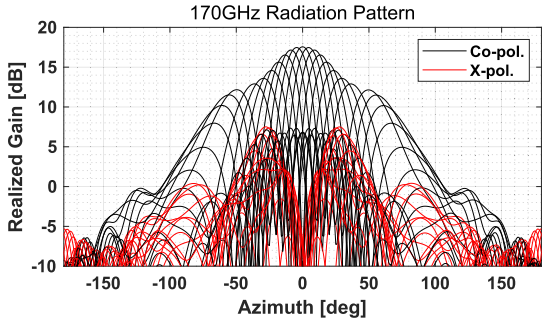

(c)

Fig. 10. Radiation patterns of antenna array at (a) 120, (b) 145, and (c) 170 GHz.

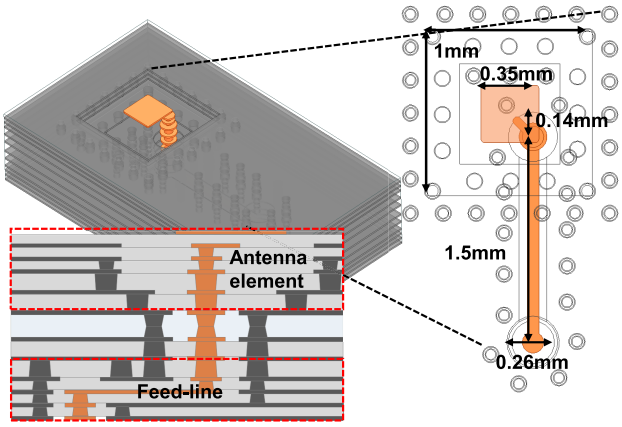

Fig. 11. Geometry of the proposed antenna with feedline (module A).

In particular, the capacitance between the capture pad and upper ground, C_{PP}, in Fig. 12(a) can be obtained by

$$C_{PP} = \frac{\varepsilon_r \varepsilon_0 \pi D_P^2}{h} \tag{3}$$

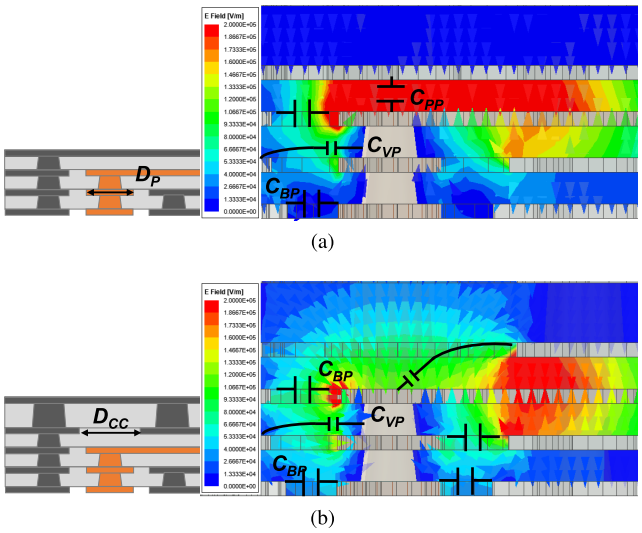

Fig. 12. E-field distribution of feedline with (a) conventional via transition and (b) proposed via transition.

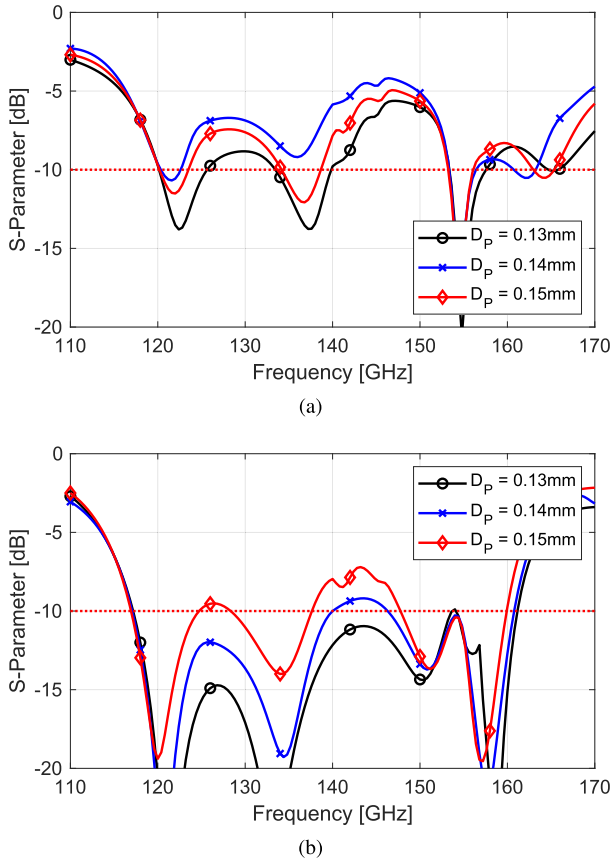

Fig. 13. S_{11} of antenna and feedline with (a) conventional via transition and (b) proposed via transition.

where D_P is the diameter of the capture pad and h is the thickness of the substrate. The capacitance should be high because of the limited capture pad size and substrate thickness. The E-field distribution of the feedline with conventional via transition is shown in Fig. 12(a), and a high field intensity is observed near the capture pad. A capped cavity, which has a hole and surrounding vias, was proposed to reduce the capacitance, as shown in Fig. 12(b). The proposed structure

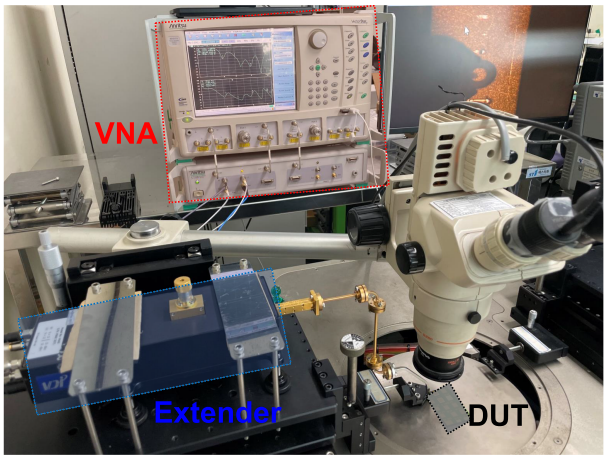

Fig. 14. Measurement setup for S_{11} of a single antenna.

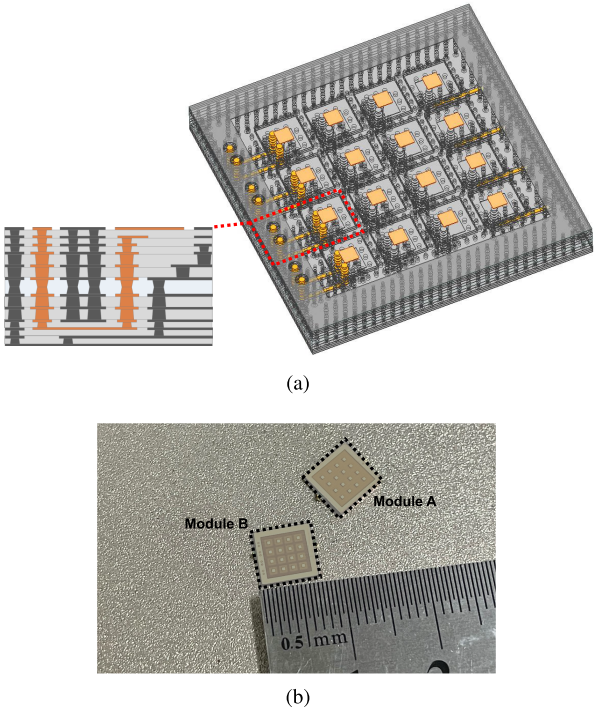

Fig. 15. (a) Layer structures and simulation model for S_{11} validation and radiation pattern (module B). (b) Photograph of the fabricated modules.

can convert C_{PP} to C_{BP} in (1), and the field intensity can be decreased significantly. The effect of the proposed transition can also be found in Fig. 13. The S_{11} values of the antenna and feedline with a conventional via transition are plotted in Fig. 13(a), which deteriorates and exhibits a narrow bandwidth. In contrast, S_{11} of the antenna and feedline with the proposed via transition in Fig. 13(b) shows better performance and a wider bandwidth of approximately 40 GHz. Fig. 13 also plots S_{11} with the variation in D_P, and the degradation of S_{11} can be confirmed by the increase in the diameter in both cases.

B. Antenna With Feedline Validation

The measurement setup for validating the antenna modules is shown in Fig. 14. A vector network analyzer (VNA) was used for measurements with waveguide-connected ground-signal-ground (GSG) probes and a frequency extension unit.

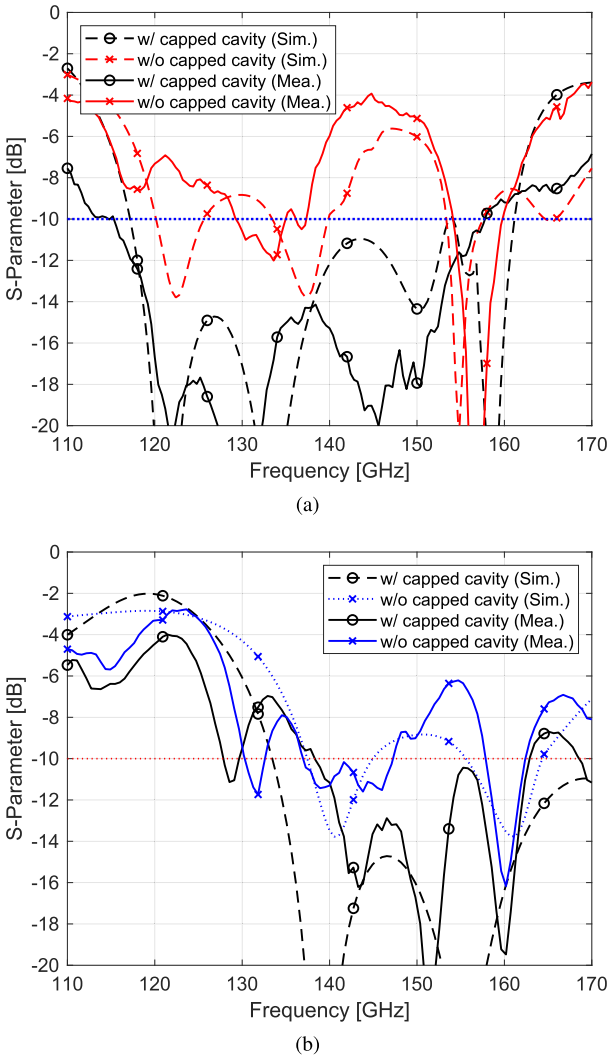

Fig. 16. Compared S_{11} of modules (a) A and (b) B.

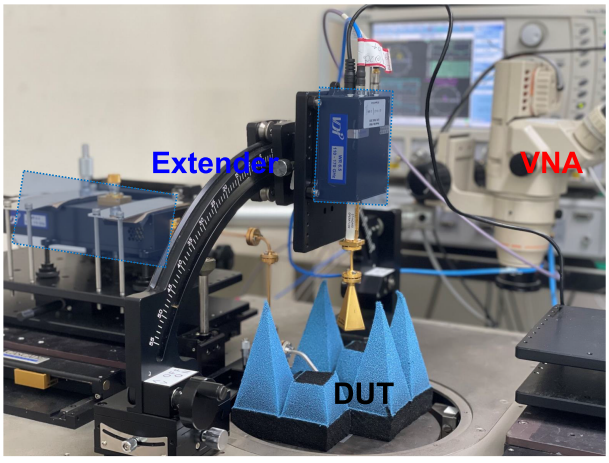

Fig. 17. Measurement setup for radiation pattern of antenna modules.

The extension unit can expand the operating range of the VNA, and frequencies from 110 to 170 GHz can be measured. Fig. 11 shows the geometry for validating the proposed antenna with a feedline. An additional cavity structure was appended between layers 2 and 5 to enhance the copper ratio by over 40% and

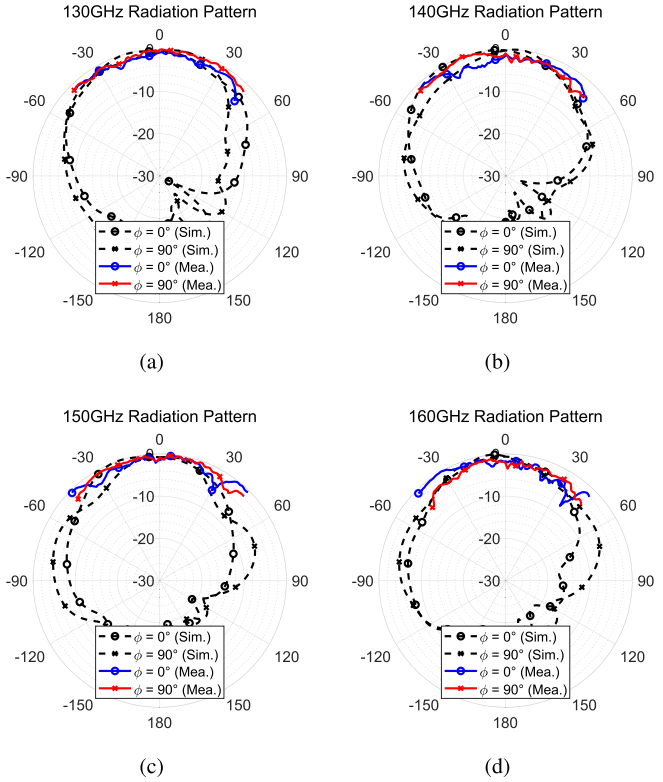

Fig. 18. Radiation patterns of antenna element with the line at (a) 130, (b) 140, (c) 150, and (d) 160 GHz.

prevent the warpage of the AiP module. Because of the effect of the feedline with the via transition and feeder position adjustment, $P_X = 0.14$ mm, and the simulated bandwidth is reduced, as shown in Fig. 13(b). The bandwidth was decreased, and the fractional bandwidth was reduced to approximately 31%. The module structure for S_{11} validation is illustrated in Fig. 11(a), and its photograph is shown in Fig. 15(b). The module could be measured on a ROHACELL foam, and the measured result shows a similar S_{11}, as shown in Fig. 16(a). The figure also shows the effects of the proposed capped cavity, which plots the bandwidth degradation without the proposed structure.

The measurement setup for the radiation pattern is illustrated in Fig. 17. The VNA is also used with GSG probes and a frequency extension unit, and a horn antenna is fixed with a jig, which can manually adjust the measurement angle from $-45°$ to $45°$. The module structure for validating the radiation pattern is illustrated in Fig. 15(a), and its photograph is shown in Fig. 15(b). Although the bandwidth is reduced to 36 GHz, as shown in Fig. 16(b), because of the via transition, S_{11} is sufficient for measuring the radiation pattern. The radiation patterns of the antenna element with the stripline are plotted for $\phi = 0°$ and $90°$ in Fig. 18. The normalized radiation patterns are plotted at 18(a) 130 GHz, 18(b) 140 GHz, 18(c) 150 GHz, and 18(d) 160 GHz. Measurements were conducted from $-45°$ to $45°$ for increments of every $1°$, and the results show a similar tendency to the simulated results. The radiation patterns of the antenna array are also plotted for $\phi = 0°$ and $90°$ in Fig. 19. The normalized radiation patterns are plotted at 140 GHz, from $-45°$ to $45°$ for measurement results.

TABLE I
COMPARISON WITH PREVIOUS STUDIES

Ref. No.	Feeding type	No. of array	f_0	BW (%)	GBW (%)	Max Gain (dBi)	Technology
[1]	CPW	Single	122	14	-	10.4	Polyimide
[9]	SIW	4×4	140	17	24	16.3	LTCC
[11]	Waveguide	Single	140	31.4	14.2	15.5	3D-print
[12]	SIW	Single	140	42.86	-	10.8	PCB
[16]	stripline	4×4	60	11.5	29	18.3	LTCC
[19]	stripline	Single	60	50.5	-	8	PCB
[21]	Microstrip	4×4	32	45	39.4	16.1	LTCC
This work	w/o line	4×4	140	55 (Sim.)	53 (Sim.)	18	PCB
	stripline	4×4	140	31 (Mea.)	-	-	PCB

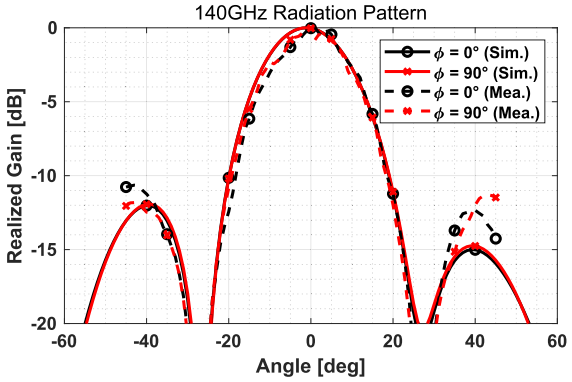

Fig. 19. Radiation patterns of the antenna array.

C. Comparison With Previous Studies

Table I presents a comparison of the performance of the proposed antenna with that of previously studied wideband antennas based on a multilayer PCB. The performance was evaluated with a −10 dB impedance bandwidth, 3 dB gain bandwidth, and the maximum realized gain. The proposed antenna array has an impedance bandwidth of more than 55%, which is higher than those reported in previous studies. In addition, a wide 3 dB gain bandwidth of more than 53% can be designed because of the stable radiation of the multimode antenna resonances. The maximum realized gain of this work is higher than that of the other four × four arrays, which is caused by the wider element spacing and higher radiation efficiency.

V. CONCLUSION

An AiP in the D-band was proposed for flip-chip technology and an integrated transceiver. The antenna configuration enables interconnection with the RFIC routed through striplines. The capacitance caused by the limited fabrication process was analyzed and overcome using the proposed capped-cavity structure. AiP prototypes with a single element and a 4 × 4 array with a power divider were fabricated and used to measure the feasibility of the PCB fabrication process and antenna performance. The proposed multimode antenna exhibited an impedance bandwidth of 55% without a stripline. An array gain of 18.1 dBi and radiation efficiency of approximately 80% were achieved for the antenna. In addition, the 3 dB gain bandwidth of the antenna array achieved a simulated impedance bandwidth of 53%.

REFERENCES

[1] S. Beer, H. Gulan, C. Rusch, and T. Zwick, "Integrated 122-GHz antenna on a flexible polyimide substrate with flip chip interconnect," *IEEE Trans. Antennas Propag.*, vol. 61, no. 4, pp. 1564–1572, Apr. 2013.

[2] R. Hasan, W. A. Ahmed, J.-H. Lu, H. J. Ng, and D. Kissinger, "*F*-band differential microstrip patch antenna array and waveguide to differential microstrip line transition for FMCW radar sensor," *IEEE Sensors J.*, vol. 19, no. 15, pp. 6486–6496, Aug. 2019.

[3] H. J. Ng, M. Kucharski, W. Ahmad, and D. Kissinger, "Multi-purpose fully differential 61-and 122-GHz radar transceivers for scalable MIMO sensor platforms," *IEEE J. Solid-State Circuits*, vol. 52, no. 9, pp. 2242–2255, Sep. 2017.

[4] S. Research. *6G Spectrum Expanding the Frontier*. Accessed: May 13, 2022. [Online]. Available: https://cdn.codeground.org/nsr/downloads/researchareas/2022May_6G_Spectrum.pdf

[5] J. Lee, H. Kim, and J. Oh, "Large-aperture metamaterial lens antenna for multi-layer MIMO transmission for 6G," *IEEE Access*, vol. 10, pp. 20486–20495, 2022.

[6] D. Seo, H. Kim, S. Oh, J. Kim, and J. Oh, "Ultrathin high-gain D-band transmitarray based on a spatial filter topology utilizing bonding layer effect," *IEEE Antennas Wireless Propag. Lett.*, vol. 21, no. 10, pp. 1945–1949, Oct. 2022.

[7] *Radio Frequency Channel/Block Arrangements for Fixed Service Systems Operating in the Bands 130–134 GHz, 141–148.5 GHz, 151.5–164 GHz and 167–174.8 GHz*, document ECC Recommendation (18)01, Apr. 2018.

[8] J. Edwin, *FCC Opens Spectrum Horizons for New Services and Technologies*, Docket 18–21, Mar. 2019.

[9] J. Xu, Z. N. Chen, X. Qing, and W. Hong, "140-GHz planar broadband LTCC SIW slot antenna array," *IEEE Trans. Antennas Propag.*, vol. 60, no. 6, pp. 3025–3028, Jun. 2012.

[10] J. Xu, Z. N. Chen, X. Qing, and W. Hong, "140-GHz TE_{20}-mode dielectric-loaded SIW slot antenna array in LTCC," *IEEE Trans. Antennas Propag.*, vol. 61, no. 4, pp. 1784–1793, Apr. 2013.

[11] C. Gu et al., "A D-band 3D-printed antenna," *IEEE Trans. Terahertz Sci. Technol.*, vol. 10, no. 5, pp. 433–442, Sep. 2020.

[12] A. Altaf, W. Abbas, and M. Seo, "A wideband SIW-based slot antenna for *D*-band applications," *IEEE Antennas Wireless Propag. Lett.*, vol. 20, no. 10, pp. 1868–1872, Oct. 2021.

[13] X. Gu, D. Liu, and B. Sadhu, "Packaging and antenna integration for silicon-based millimeter-wave phased arrays: 5G and beyond," *IEEE J. Microw.*, vol. 1, no. 1, pp. 123–134, Jan. 2021.

[14] H. Kim and S. Nam, "Performance enhancement of 5G millimeter wave antenna module integrated tablet device," *IEEE Trans. Antennas Propag.*, vol. 69, no. 7, pp. 3800–3810, Jul. 2021.

[15] T. Joo, C. Hwang, J. Park, K. Kim, and J. Jung, "Design of a tile-type Rx multi-beam digital active phased array antenna system," *J. Electromagn. Eng. Sci.*, vol. 22, no. 1, pp. 12–20, Jan. 2022.

[16] L. Wang, Y. X. Guo, and W. X. Sheng, "Wideband high-gain 60-GHz LTCC L-probe patch antenna array with a soft surface," *IEEE Trans. Antennas Propag.*, vol. 61, no. 4, pp. 1802–1809, Apr. 2013.

[17] J. Seo et al., "Miniaturized dual-band broadside/endfire antenna-in-package for 5G smartphone," *Proc. IEEE Trans. Antennas Propag.*, vol. 69, no. 12, pp. 8100–8114, Dec. 2021.

[18] M. Li and K.-M. Luk, "Low-cost wideband microstrip antenna array for 60-GHz applications," *IEEE Trans. Antennas Propag.*, vol. 62, no. 6, pp. 3012–3018, Jun. 2014.

[19] M. Li and K.-M. Luk, "Wideband magneto-electric dipole antenna for 60-GHz millimeter-wave communications," *IEEE Trans. Antennas Propag.*, vol. 63, no. 7, pp. 3276–3279, Jul. 2015.

[20] Y. Li and K.-M. Luk, "A 60-GHz wideband circularly polarized aperture-coupled magneto-electric dipole antenna array," *IEEE Trans. Antennas Propag.*, vol. 64, no. 4, pp. 1325–1333, Apr. 2016.

[21] Y. Li, C. Wang, and Y. X. Guo, "A Ka-band wideband dual-polarized magnetoelectric dipole antenna array on LTCC," *IEEE Trans. Antennas Propag.*, vol. 68, no. 6, pp. 4985–4990, Jun. 2020.

[22] H. Aliakbari, M. Mosalanejad, C. Soens, G. A. Vandenbosch, and B. K. Lau, "Wideband SIW-based low-cost multilayer slot antenna array for E-band applications," *IEEE Trans. Compon., Packag., Manuf. Technol.*, vol. 9, no. 8, pp. 1568–1575, Aug. 2019.

[23] G. Hernandez-Sosa, R. Torres-Torres, and A. Sanchez, "Impedance matching of traces and multilayer via transitions for on-package links," *IEEE Microw. Wireless Compon. Lett.*, vol. 21, no. 11, pp. 595–597, Nov. 2011.

[24] I. Ndip et al., "Modeling, quantification, and reduction of the impact of uncontrolled return currents of vias transiting multilayered packages and boards," *IEEE Trans. Electromagn. Compat.*, vol. 52, no. 2, pp. 421–435, May 2010.

[25] M. Friedrich, M. Leone, and C. Bednarz, "Exact analytical solution for the via-plate capacitance in multiple-layer structures," *IEEE Trans. Electromagn. Compat.*, vol. 54, no. 5, pp. 1097–1104, Oct. 2012.

[26] H. Lim, D.-H. Lee, J. Kim, and S. Hong, "Spectroscopic sensing method of liquid permittivity with on-chip capacitor," *J. Electromagn. Eng. Sci.*, vol. 22, no. 1, pp. 28–33, Jan. 2022.

[27] H. Xu, J. Zhou, K. Zhou, Q. Wu, Z. Yu, and W. Hong, "Planar wideband circularly polarized cavity-backed stacked patch antenna array for millimeter-wave applications," *IEEE Trans. Antennas Propag.*, vol. 66, no. 10, pp. 5170–5179, Oct. 2018.

[28] H. Kim et al., "60 GHz digitally controllable and sequentially rotated fed antenna array," *Electron. Lett.*, vol. 53, no. 13, pp. 821–822, 2017.

[29] M. Stanley et al., "A dual-band dual-polarised stacked patch antenna for 28 GHz and 39 GHz 5G millimetre-wave communication," in *Proc. 13th Eur. Conf. Antennas Propag. (EuCAP)*, Mar./Apr. 2019, pp. 1–4.

[30] I.-J. Hwang, H.-W. Jo, B. K. Ahn, J.-I. Oh, and J.-W. Yu, "Cavity-backed stacked patch array antenna with dual polarization for mmWave 5G base stations," in *Proc. 13th Eur. Conf. Antennas Propag. (EuCAP)*, Mar./Apr. 2019, pp. 1–5.

[31] S. Bhardwaj and Y. Rahmat-Samii, "Revisiting the generation of cross-polarization in rectangular patch antennas: A near-field approach," *IEEE Antennas Propag. Mag.*, vol. 56, no. 1, pp. 14–38, Feb. 2014.

[32] Y. Kim, H. Kim, I. Yoon, and J. Oh, "4×8 patch array-fed FR4-based transmit array antennas for affordable and reliable 5G beam steeringFR4-based transmit array antennas for affordable and reliable 5G beam steering," *IEEE Access*, vol. 7, pp. 88881–88893, 2019.

[33] Y. He and Y. Li, "Dual-polarized microstrip antennas with capacitive via fence for wide beamwidth and high isolation," *IEEE Trans. Antennas Propag.*, vol. 68, no. 7, pp. 5095–5103, Jul. 2020.

[34] Y. Li, Z. N. Chen, X. Qing, Z. Zhang, J. Xu, and Z. Feng, "Axial ratio bandwidth enhancement of 60-GHz substrate integrated waveguide-fed circularly polarized LTCC antenna array," *IEEE Trans. Antennas Propag.*, vol. 60, no. 10, pp. 4619–4626, Oct. 2012.

Hyunjin Kim (Member, IEEE) received the B.S. degree in electronic engineering from Korea University, Seoul, South Korea, in 2006, and the M.S. and Ph.D. degrees in electrical engineering from Seoul National University, Seoul, in 2009 and 2021, respectively.

From 2009 to 2020, he was a Staff Engineer at Samsung Electronics, Suwon, South Korea, responsible for research on advanced antenna technologies for communications, advanced network devices, and mmWave antenna systems. He is currently a Post-Doctoral Research Fellow at the Department of Electrical and Computer Engineering, Institute of New Media and Communications, Seoul National University. His research interests include D-band antenna design, mmWave array antenna systems, and metasurfaces.

Jungsuek Oh (Senior Member, IEEE) received the B.S. and M.S. degrees from Seoul National University, Seoul, South Korea, in 2002 and 2007, respectively, and the Ph.D. degree from the University of Michigan, Ann Arbor, MI, USA, in 2012.

From 2007 to 2008, he worked with Korea Telecom, Seongnam, South Korea, as a Hardware Research Engineer, working on the development of flexible RF devices. In 2012, he was a Post-Doctoral Research Fellow at the Radiation Laboratory, University of Michigan. From 2013 to 2014, he was a Staff RF Engineer with Samsung Research America, Dallas, TX, USA, working as a Project Leader for the 5G/millimeter-wave antenna system. From 2015 to 2018, he was a Faculty Member with the Department of Electronic Engineering, Inha University, Incheon, South Korea. He is currently an Associate Professor at the School of Electrical and Computer Engineering, Seoul National University. He has published over 50 technical journals and conference papers. His research areas include mmWave beam focusing/shaping techniques, antenna miniaturization for integrated systems, and radio-propagation modeling for indoor scenarios.

Dr. Oh was a recipient of the 2011 Rackham Predoctoral Fellowship Award at the University of Michigan. He has served as a TPC Member and the Session Chair for the IEEE AP-S/USNC-URSI and ISAP. He has served as a Technical Reviewer for IEEE TRANSACTIONS ON ANTENNAS AND PROPAGATION and IEEE ANTENNAS AND WIRELESS PROPAGATION LETTERS.